Cleaner Engineering and Technology 31 (2026) 101147

Contents lists available at ScienceDirect

Cleaner Engineering and Technology

journal homepage: www.sciencedirect.com/journal/cleaner-engineering-and-technology

Highly efficient photocatalytic conversion of CO_2 to hydrocarbons using visible-active co-doped TiO_2/ PDMS nanocomposite

Majed Bahadorian [a], Farzaneh Arabpour Roghabadi [a,b,*], Vahid Ahmadi [b], Afsanehsadat Larimi [c]

[a] Department of Process Engineering, Faculty of Chemical Engineering, Tarbiat Modares University, Tehran, Iran
[b] Optoelectronics and Nanophotonics Research Group, Faculty of Electrical and Computer Engineering, Tarbiat Modares University, Tehran, Iran
[c] School of Engineering and Applied Sciences, Department of Chemical Engineering, Swansea University, Wales, UK

ARTICLE INFO

Keywords:
Polydimethylsiloxane
Co-doping
Titanium dioxide
Photocatalytic reduction
Carbon dioxide

ABSTRACT

Considering the rising emission of the carbon dioxide (CO_2) and its detrimental effects on the environment, conversion of CO_2 into value-added products has emerged as a critical area of research. In particular, the photocatalytic reduction of CO_2 into fuels using solar energy has recently attracted significant attention. In this study, a nanocomposite of co-doped titanium dioxide (TiO_2) nanoparticles with polydimethylsiloxane (PDMS) is utilized for photocatalytic reduction of CO_2. Photo, chemical, and thermal-stable PDMS serves as a transparent flexible binder for photocatalyst nanoparticles, facilitating their usage and recycling. To make TiO_2 photocatalysts visible-active, reduce the charge recombination rate, and improve the charge transport and lifetime, they are co-doped using nonmetal nitrogen (N) and metal silver (Ag) with different concentrations. Following the optical, morphological, and structural analysis of the photocatalysts, their photocatalytic performance is evaluated in a fixed gas bed photoreactor. The TiO_2 photocatalyst shows the lowest yield for methane (3.2 μmol/g catalyst) and ethane (0.42 μmol/g catalyst). While, the yield for methane and ethane using Ag-N-TiO_2 photocatalyst reaches 34.42 and 1.01 μmol/g catalyst, respectively. Remarkably, when the PDMS-Ag-N-TiO_2 nanocomposite is employed, the highest methane and ethane yield of 122.21 and 10.22 μmol/g catalyst are achieved, respectively. Thus, in the presence of PDMS polymer, instantaneous quadrupolar interactions occur between its siloxane groups and carbon dioxide molecules. This promotes the adsorption of greater amounts of CO_2, making it more available for the photocatalytic reduction reaction and thereby enhancing hydrocarbon production.

1. Introduction

Since the Industrial Revolution, atmospheric carbon dioxide (CO_2) levels have increased from 280 ppm to approximately 430 ppm, exceeding the safe threshold of 350 ppm. This rise, primarily driven by fossil fuel combustion, has led to global warming, environmental degradation, and serious threats to ecosystems, necessitating urgent and effective mitigation efforts (Asadi et al., 2022; Zheng et al., 2024). In recent years, researchers have begun exploring various methods for CO_2 utilization and transformation, including photocatalytic reduction of CO_2, electrochemical, thermal, biochemical, and chemoenzymatic approaches. Photocatalytic technology is a more energy-efficient and sustainable technique compared to other approaches such as electrochemical and thermal methods. With its significant potential to reduce environmental pollution, it offers an effective solution to the energy crisis while promoting sustainable fuel sources. In contrast to thermally driven pathways, photocatalytic CO_2 conversion can proceed under ambient temperature and pressure, avoiding additional energy input. (Saravanan et al., 2021; Ahmadi et al., 2023). The photocatalytic reduction of CO_2 utilizing semiconductors, represents a clean method for the conversion of greenhouse gas into hydrocarbon fuels. The photogenerated electrons reduce CO_2 (often in the presence of H_2O) to products such as methane (CH_4), ethane (C_2H_6), methanol (CH_3OH), and carbon monoxide (CO), while the holes oxidize water or surface-adsorbed species (Garcia et al., 2025).

Solar-based technologies, such as photo-Fenton and photocatalytic methods, have emerged as promising solutions to address ronmental pollution and energy crises. The photo-Fenton process, as a member of the advanced oxidation processes (AOPs), employs solar irradiation to drive the Fe^{2+}/Fe^{3+} redox couple in the presence of hydrogen peroxide,

* Corresponding author. Department of Process Engineering, Faculty of Chemical Engineering, Tarbiat Modares University, Tehran, Iran.
E-mail address: Arabpour@modares.ac.ir (F. Arabpour Roghabadi).

https://doi.org/10.1016/j.clet.2026.101147
Received 13 October 2025; Received in revised form 8 January 2026; Accepted 8 January 2026
Available online 2 February 2026

thereby producing highly reactive radical species (Janani et al., 2025). AOPs have gained considerable recognition as highly effective and adaptable methods, attracting widespread interest in diverse disciplines because of their effectiveness and environmental sustainability. These processes have shown remarkable potential in various applications, including hydrogen generation, CO_2 reduction, wastewater treatment, and microbial disinfection (Khan et al., 2025; Safa et al., 2025).

Among the various semiconductors used as photocatalysts, titanium dioxide (TiO_2), an n-type semiconductor, is widely employed for CO_2 photoreduction. Its conduction band edge is sufficiently negative to drive the reduction of CO_2, while its valence band is positive enough to oxidize water, and it also exhibits excellent chemical stability, non-toxic nature, abundance, and low cost. These features have made TiO_2 one of the most extensively studied photocatalysts for solar-driven CO_2 conversion. However, it suffers from some challenges, especially its high bandgap (~3.2 eV), which results in the absorption of only 3–4% of the solar spectrum in the ultra-violet (UV) range (Guo et al., 2020; Cui et al., 2022).

To enhance photocatalytic performance, various strategies have been developed, including defect engineering, heterostructure construction, surface modification, and activator-assisted catalysis. For example, in activator-assisted photocatalysis, peroxymonosulfate (PMS) is employed to generate reactive oxygen species (ROS) that accelerate degradation reactions, while $NaBH_4$ which provides electrons to facilitate redox reactions and enhance catalytic efficiency (Sre et al., 2025; Steffy et al., 2025). In addition, To extend its optical response into the visible region and improve charge separation, bandgap engineering through metal and non-metal doping has been widely investigated. Doping introduces impurity or defect states within the bandgap, which can narrow the effective bandgap and act as trapping sites that facilitate spatial separation of photogenerated electron-hole (Piątkowska et al., 2021; Bahadorian et al., 2025). Thus far, TiO_2 photocatalyst has been doped by nonmetals, including nitrogen (N) (Ahmadi et al. 2024), carbon (C) (Wang et al., 2017), phosphorus (P) (Deng et al., 2021), and fluorine (F) (Diao et al., 2022). Among various non-metal dopants, nitrogen is particularly attractive for visible-light-driven TiO_2 photocatalysis because its covalent radius, electronegativity, and ionization energy are comparable to those of oxygen, which facilitates substitutional incorporation on oxygen sites and promotes effective hybridization between N 2p and O 2p states in the valence band. In addition, the abundance and low cost of nitrogen precursors, together with the good thermal stability of N-doped TiO_2 under typical synthesis and operating conditions, make nitrogen a practical and scalable dopant for enhancing photocatalytic performance (Divya et al., 2022; Subhiksha et al., 2025). As reported, N-doping of TiO_2 noticeably improved photocatalytic activity for the dynamic reduction of CO_2 to CO. The N- doped TiO_2 nanophotocatalyst is synthesized using a sol-gel method and loaded onto cordierite honeycomb monoliths. N- doped TiO_2 reduced the TiO_2 band gap from 3.12 eV to 3.06 eV, and exhibited 4.67 times higher CO production compared to pure TiO_2 (56 vs. 12 μmol g-catal^{-1}. h^{-1}) (Tahir and Tahir, 2016). Incorporating noble metals, including gold (Au) (Khairy et al., 2022), silver (Ag) (Nagaraj et al., 2021), platinum (Pt) (Jing et al., 2022), copper (Cu) (Raguram and Rajni, 2022), and palladium (Pd) (Jahdi et al., 2020), into TiO_2 is a viable approach to enhance charge transfer efficiency by facilitating electron trapping, reducing electron-hole recombination, and extending light absorption into the visible range, thereby significantly improving photocatalytic performance. Among these metals, silver is particularly attractive for practical applications because it combines a strong plasmonic response in the visible range with a comparatively lower cost and facile synthesis (Steffy et al., 2025). Kang et al. synthesized reduced graphene oxide (rGO)-wrapped Ag-TiO_2 nanofibers (NFs) with a coaxial electrospinning method. Upon exposure to visible light, rGO/Ag/TiO_2 NFs showed a 25-fold enhancement in the conversion of CO_2 to CH_4 relative to bare TiO_2 NFs, yielding 4.301 μmol g_{NF}^{-1} of CH_4 for a duration of 7 h. Furthermore, Ag-TiO_2 NFs (without rGO) demonstrated approximately 7 times higher efficiency than pure TiO_2 NFs. Ag doping enhanced photocatalytic performance by facilitating Fermi level equilibration, serving as a sink for photogenerated electrons, offering catalytic sites for adsorbed species and reaction intermediates, and increasing visible light absorption through localized surface plasmon resonance (LSPR) (Kang and Hwang, 2022). In photocatalytic processes, suitable supports can significantly improve activity and selectivity by increasing the accessible surface area, facilitating mass transfer, preventing nanoparticle agglomeration, and enabling convenient catalyst recovery and reuse (Ali et al., 2023). Among various types of supports, polymeric ones have attracted considerable attention due to their structural flexibility, chemical properties tunability, suitable stability, and compatibility with diverse environments. Using suitable polymeric support, the adsorption and transport behavior of reactant molecules can be controlled (Srikanth et al., 2017; Sosnin et al., 2021). Polydimethylsiloxane (PDMS) is a silicone polymer with distinctive characteristics that has garnered significant interest in photocatalysis and it is one of the suitable candidates for optical applications. This polymer, characterized by its flexible structure, optical transparency, biocompatibility, robust thermal stability, high chemical stability, and appropriate permeability to CO_2, demonstrates considerable potential in enhancing photocatalytic processes. The capacity of PDMS to form a flexible and gas-permeable matrix, together with its potential to enhance the local concentration of CO_2, introduces this polymer as a suitable support for photocatalytic CO_2 reduction systems (Ali et al., 2023; Ali et al., 2024).

Although previous studies have explored the individual photocatalytic activities of N-doped TiO_2 and silver, comprehensive research on their combined performance across different doping levels remains limited. Co-doping involves the simultaneous doping of metal cations, anions, or metal/non-metal elements, in contrast to single doping. Furthermore, photocatalytic CO_2 reduction is often conducted using powdered catalysts, which can suffer from limited gas-solid contact, and nanoparticle agglomeration. These factors restrict CO_2 availability near active sites.

In this work, an efficient TiO_2-based photocatalytic system is introduced for CO_2 reduction. To tune the energy levels of the TiO_2 and make it visible-active, it is doped with N and Ag simultaneously. The effects of varying concentrations of N and Ag dopants on the photocatalytic performance of TiO_2 are systematically investigated, with a focus on the reduction of CO_2 to methane and ethane, while transparent PDMS is employed as a CO_2-philic, gas-permeable support to concentrate CO_2 around the photocatalyst nanoparticles. The integration of modified TiO_2 with PDMS aims to enhance photocatalytic efficiency and provide new insights into material design for CO_2 conversion.

2. Experimental

2.1. Materials

TiO_2 utilized in this study is a commercial product (P25) sourced from Evonik Company, exhibiting a stated purity of 99.5%. Urea with a purity of 99%, silver nitrate ($AgNO_3$) with a purity of 99.9%, and sodium hydroxide with a purity of 97% are purchased from Merck. PDMS (Sylgard 184 A) and its curing agent (Sylgard 184 B) are obtained from Dow Corning Company (U.S.A.). The study employs ethanol with a purity of 96% (Kimia Alcohol Zanjan Company). All materials are utilized without purification.

2.2. Preparation of photocatalysts

2.2.1. Doping of TiO_2 with nitrogen

A mixture of urea and TiO_2 is initially prepared with molar ratios of 5:1.5, 5:3, and 5:5, TiO_2: urea. The mixture is subsequently mixed with 50 mL of deionized water and subjected to vigorous stirring for 2 h. The resulted mixtures are labeled as 1.5 N-TiO_2, 3 N-TiO_2, and 5 N-TiO_2,

reflecting the varying molar ratios employed. The sample is then exposed to a temperature of 100 °C to promote water evaporation. Subsequent to the milling process, the powders are subjected to calcination at a temperature of 400 °C for 1 h (Marques et al., 2019).

2.2.2. Doping of TiO_2 with silver

Ag-TiO_2 nanoparticles are prepared using $AgNO_3$ as the precursor for the silver component. 0.6 g of TiO_2 nanoparticles are added to 100 mL of $AgNO_3$ solution at concentrations of 0.5, 1, and 3 mM. The mixture is stirred at a rate of 500 rpm for a period of 1 h at room temperature (RT). The resultant mixtures are labeled as 0.5Ag-TiO_2, 1Ag-TiO_2, and 3Ag-TiO_2, reflecting the various molar ratios employed. The pH of the suspension is adjusted to 7 using a 0.1 M NaOH solution to improve the adsorption of Ag onto TiO_2. Upon achieving Ag sorption equilibration, the solution is filtered to separate the Ag-TiO_2 from the liquid phase. Thereafter, the Ag-TiO_2 undergoes four cycles of washing with ethanol and deionized water to remove any weakly bound and/or undoped Ag on the TiO_2 surface. The nanoparticles are subsequently dried in an oven at 100 °C for 12 h (Ali et al., 2024).

2.2.3. Co-doping of TiO_2 with nitrogen and silver

The 1.5 N-TiO_2 sample is initially prepared as explained in Section 2.2.1, followed by doping with silver at a concentration of 0.5 mM as mentioned in Section 2.2.2. The nanoparticles are briefly labeled as Ag-N-TiO_2.

2.2.4. Preparation of PDMS composite with Ag-N-TiO_2

Initially, 0.1 g of Ag-N-TiO_2 powder is mixed with 0.95 g of n-hexane and ultrasonicated for 15 min. Then, 0.91 g of Part A PDMS polymer is added into the initial solution. To mix the powder and polymer, the solution is ultrasonicated again. To remove the n-hexane solvent, the solution is placed in a vacuum oven at 50 °C for 30 min. Subsequently, 0.09 g of Part B polymer is added into the solution and thoroughly stirred using a shaker (Ali et al., 2024). To perform the photoreaction test, the solution is transferred into a glass container until a thin film is formed inside the container. Then, the container is positioned in the center of the photoreactor for the performance test.

2.3. Characterization techniques

Fourier-Transform Infrared (FTIR) analysis (Spectrum One, USA) is employed to identify the functional groups present in the samples. X-ray diffraction (XRD) (Rigaku Ultima IV, Japan) is used to determine the crystalline phase of the materials. Field-Emission scanning electron microscopy (FESEM, TESCAN, Czech Republic) and energy-dispersive X-ray spectroscopy (EDS) analysis are used to study the materials composition and morphology. Using an Avantes (AvaLight-DHS) UV–Vis spectrophotometer, the optical properties of the materials are recorded. A fluorescence spectrophotometer is used to obtain photoluminescence (PL) spectra of materials (Varian Cary Eclipse, USA). In the Brunauer-Emmett-Teller (BET) analysis, the total pore volume, average pore size, and specific surface area (S_{BET}) of the materials are measured by N_2 physisorption at 77 K utilizing Belsorp mini II equipment manufactured in Japan.

2.4. CO_2 photoreduction in photoreactor

Photocatalytic CO_2 reduction tests are performed in a fixed gas bed photoreactor at 1 bar pressure and 25 °C. A 200 mL Pyrex photoreactor with a quartz window on the top to enhance light transmission to the photocatalyst surface is utilized. A UV–visible 250 W mercury vapor lamps ($\lambda > 350$ nm), with average irradiance of 280 W/m^2, is positioned 5 cm from the window at the top of the photoreactor. Initially, 0.1 g of photocatalyst powder is dispersed in 10 mL of deionized water and then heated to form a thin layer of photocatalyst on a glass plate. It is subsequently positioned at the center of the photoreactor. The preparation of the PDMS and Ag-N-TiO_2 composite for the photoreactor test is also discussed in Section 2.2.4. Before lighting the lamp, a continuous flow of 99.99% high-purity CO_2 gas is injected into the photoreactor for 1 h at a flow rate of 50 mL/min to remove air and impurities. After that, the CO_2 gas flow passes through a bubbler containing deionized water for 30 min to introduce humidified CO_2 gas as the input feed into the photoreactor. After the photoreactor is filled with humidified CO_2, all outlets are sealed and the lamp is lit. After 8 h from the start of the reaction, a 1 mL sample is taken from the photoreactor for analysis using a syringe. The syringe is then injected into a gas chromatograph (Agilent 7890 B) equipped with an ionization detector (FID) for gas sample analysis (Ahmadi et al. 2024). To ensure that the products obtained are only the result of photocatalytic reduction of CO_2, a number of experiments are performed under the following conditions: 1) no radiation 2) no photocatalyst 3) no CO_2 gas 4) pure PDMS. Ultimately, no products are observed in these 4 experiments. To ensure the reliability of the photocatalytic performance evaluation, experiments are repeated three times under identical conditions, showing an experimental error of less than 1%

3. Results and discussion

To understand the effect of the single and co-doping on the optical properties of the photocatalysts, the UV–visible absorbance spectra of the samples are recorded and depicted in Fig. 1(a). Moreover, the optical bandgap for different samples is estimated using the Tauc plot as (Bhatkhande et al., 2002).

$$(\alpha h\nu) = \mathrm{A}\left(h\nu - E_g\right)^n \tag{1}$$

$$h\nu = \frac{1240}{\lambda} \tag{2}$$

where α represents the absorption coefficient, $h\nu$ denotes the photon energy, A is a constant determined by the effective electron-hole mass, E_g the optical band gap energy, n can be values of 0.5 or 2, and λ the incident light wavelength. To compare the bandgap between undoped and doped TiO_2 with N and Ag, the extracted results from UV–visible spectra are also displayed in Table 1.

Fig. 1(a) indicates that pure TiO_2 nanoparticles are UV-active. In photocatalysts doped with N and Ag, expanding the optical absorption into the visible region is evident. The results align with the color alteration of the samples (Fig. 1(c)). Table 1 indicates that N-doping results in a reduction of the band gap relative to pure TiO_2, signifying effective doping. The most probable mechanism that explains the observed light absorption may be the oxygen vacancy generated by the thermal treatment. Through the doping of N atoms into the TiO_2 lattice, the N 2p states contribute to the narrowing the bandgap via mixing with O 2p states. The narrower bandgap expands the photon absorption spectrum and promotes the excitation of an electron from the valence band to the conduction band in the doped semiconductor, consequently enhancing the photocatalytic activity of the material (Wang et al., 2005; Zhang et al., 2021). Furthermore, doping with Ag causes a shift in the light absorption edge to the longer wavelengths. Ag clusters can provide the formation of localized energy levels within the band gap of TiO_2, improving the light absorption (Zhang et al., 2021).

To evaluate the crystalline structure of the photocatalysts and the doping effects, the X-ray diffraction pattern of the pure TiO_2 and doped samples are presented in Fig. 2(a). The XRD peaks of the samples include two crystalline phases, anatase and rutile, with anatase being the predominant phase. The X-ray diffraction peaks of the prepared samples are observed at $2\theta = 25.3°$, 36.9°, 37.7°, 38.5°, 48°, 53.8°, 55°, 62.6°, 68.7°, 70.2°, 75°, and 76°, corresponding to the miller indices (101), (103), (004), (112), (200), (105), (211), (204), (116), (220), (215), and (301), respectively, and are in accordance with the standard of the anatase phase of TiO_2 (JCPDS 78–2486) (Gegova et al., 2015). The X-ray

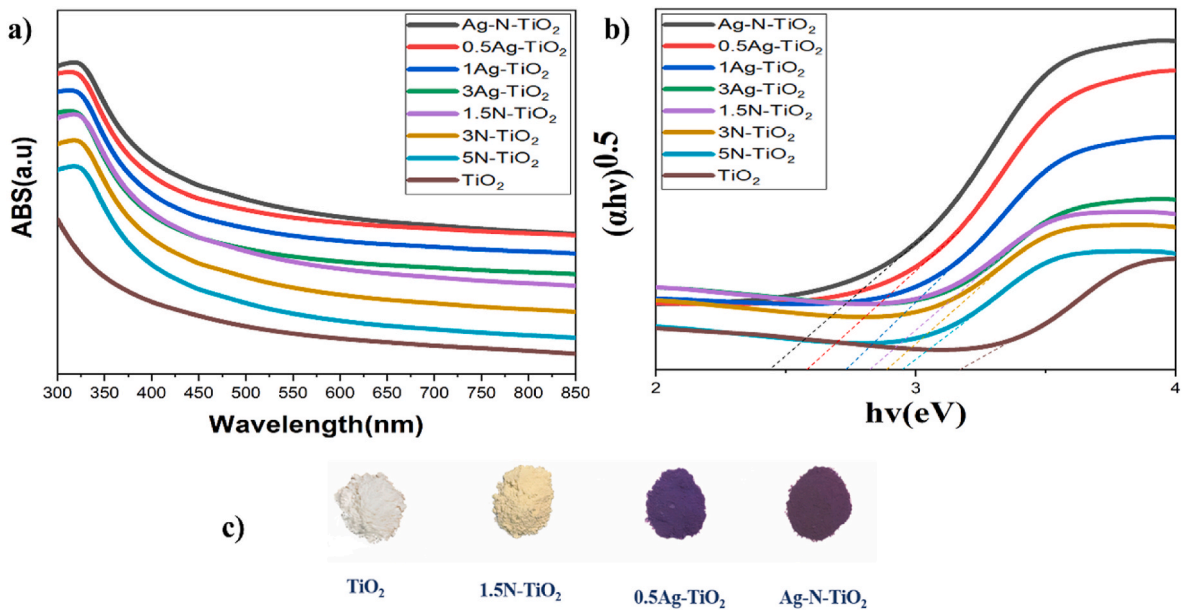

Fig. 1. (a) UV–vis absorption spectra of photocatalyst samples, (b)Tauc plot of pure TiO_2 and modified samples (c) the color of the different samples.

Table 1
Bandgap results obtained from the Tauc plot of the samples.

Photocatalyst	Band gap (eV)
TiO_2	3.21
1.5 N-TiO_2	2.77
3 N-TiO_2	2.81
5 N-TiO_2	2.93
0.5Ag-TiO_2	2.58
1Ag-TiO_2	2.74
3Ag-TiO_2	2.77
Ag-N-TiO_2	2.43

diffraction peaks observed at 2θ values of 27.4°, 36.0°, 39.1°, 41.2°, 56.6°, and 62.7° correspond to the miller indices (110), (101), (200), (111), (220), and (002), respectively, and are indicative of the rutile phase of TiO_2 (JCPDS 89–4202) (Karunakaran et al., 2011).

Fig. 2(a) shows no impurity phase after N-doping, suggesting that N atoms are located in the interstitial and substitutional sites of the TiO_2 crystal lattice. Furthermore, it depicts that the diffraction peak positions of N-doped TiO_2 samples closely resemble those of pure TiO_2 nanoparticles. However, a further examination of the major anatase peak on the (101) plane reveals a minor shift towards higher angles for N-doped samples (Fig. 2(b)). The shifts signify an increase in oxygen vacancies resulting from nitrogen impurity substitution in the TiO_2 lattice (Selvaraj et al., 2013; Li et al., 2015; Deshmukh et al., 2021). The diffraction patterns of the TiO_2 sample doped with Ag dose not exhibit a distinct Ag peak (Fig. 2(a)). It can be attributed to the low doping concentration of Ag within the TiO_2 nanoparticles. The ionic radius of the Ag cation (Ag^+) is roughly 126 Pm, significantly larger than that of the titanium cation (Ti^{4+}), which measures approximately 68 Pm. Consequently, it can be inferred that a minimal quantity of Ag^+ ions infiltrates the TiO_2 crystal lattice (Yuan et al., 2010; Santos et al., 2015).

The mean anatase crystallite size of all samples is determined from the full width at half maximum (FWHM) of the principal anatase diffraction peaks using Debye-Scherrer method. Before N-doping, the average crystallite size of TiO_2 is 20.4 nm. After N-doping, it drops to 19.8, 19.5, and 19.4 nm for the 1.5 N-TiO_2, 3 N-TiO_2, and 5 N-TiO_2 samples, respectively. The average TiO_2 crystal size after Ag-doping is determined to be 17.7 nm, 17.6 nm, and 17.3 nm for the 0.5Ag-TiO_2, 1Ag-TiO_2, and 3Ag-TiO_2 samples, respectively.

FESEM images of the TiO_2, 1.5 N-TiO_2, 0.5Ag-TiO_2, Ag-N-TiO_2, and PDMS-Ag-N-TiO_2 samples are presented in Fig. 3, showing no significant changes after the doping. Further, suitable dispersion of nanoparticles in PDMS matrix is observed.

The elemental composition of the Ag-N-TiO_2 nanoparticles are examined by mapping and EDS analysis, and the results are shown in Fig. 4. The mapping images indicate acceptable distribution of elements (Fig. 4 (a)). The EDS spectrum confirms the presence of Ti, O, Ag, and N in the Ag-N-TiO_2 sample with weight percentages (wt.%) of 54.45%, 44.4%, 0.48%, and 0.67%, respectively (Fig. 4 (b)). The intensity of the peaks attributed to Ag and N are negligible due to their low concentration in the TiO_2 matrix. No significant signal from other elements is observed, suggesting the high purity of the synthesized photocatalyst.

Nitrogen gas (N_2) adsorption-desorption analysis is conducted to examine the influence of N and Ag doping on the surface area and porosity of the prepared photocatalysts. Fig. 5 illustrates the N_2 adsorption-desorption isotherms of undoped TiO_2 photocatalyst and doped samples with varying loadings. The BET surface area data for all samples are presented in Table 2. It can be seen that all the photocatalysts follow the type (IV) isotherm physical adsorption isotherm according to the IUPAC physical adsorption isotherm classification and have a type H3 hysteresis loop at high relative pressures ($P/P_0 \approx$ 0.8–9.0), indicating a mesoporous material with low porosity. Table 2 indicates that N-doping positively influences the specific surface area of TiO_2. In the N-doped samples, the 1.5 N-TiO_2 sample has the highest surface area, which can increase the effective interaction between the photocatalyst and the reactant. In fact, it can be stated that the higher the surface area, the better the photocatalyst activity. The specific surface area also decreases with increasing N-doping concentration. A similar trend of reduced specific surface area is seen in samples with elevated Ag concentrations, possibly attributable to particle aggregation on the surface and obstruction of active sites resulting from increased doping agent loading (Sirivallop et al., 2020).

As Fig. 6(a) shows all four samples exhibit similar vibrations in the infrared band. The high intensity and broad peak in the low wavelength region of 400 cm^{-1} to 900 cm^{-1} is attributed to the strong stretching vibrations of Ti-O and Ti-O-Ti bonds (Sun et al., 2018). The two peaks at 3000 cm^{-1} to 3600 cm^{-1} and 1620 cm^{-1} are attributed to the stretching vibration of the hydroxyl group on the surface and the bending O-H bond of water molecules, respectively (Yuan et al., 2010; Beshtar et al., 2024). Notably, in comparison with the pure TiO_2, the intensity of the

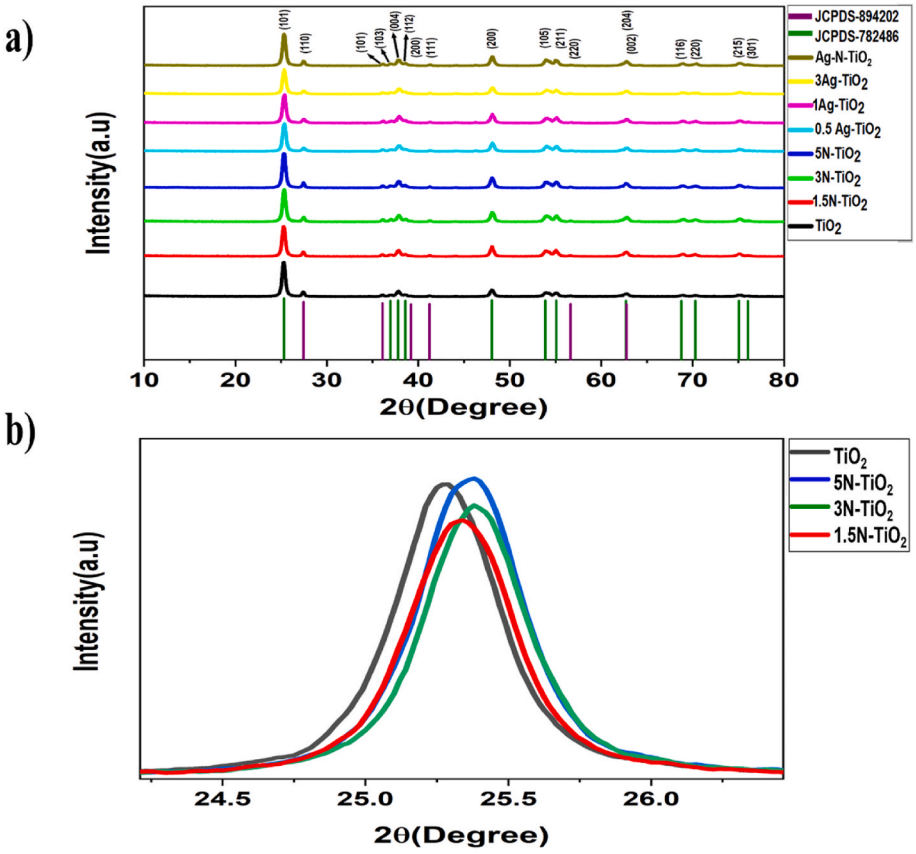

Fig. 2. (a) XRD patterns of pure TiO_2 and doped samples compared to the standard reference (b) The minor changes in the (101) plane of the anatase phase occurred due to the N-doping.

two absorption peaks associated with the hydroxyl group and water molecules is stronger in the prepared N-TiO_2 sample. This indicates that the N-TiO_2 sample has more surface-adsorbed water and hydroxyl groups, which are crucial for photocatalytic reactions. On the other hand, the hydroxyl groups on the surface of the photocatalyst, enhance photocatalytic activity through their interactions with photogenerated holes, which provide better charge transfer and inhibit the recombination of electron-hole pairs (Selvaraj et al., 2013; Cheng et al., 2016). The peak at 1025 cm^{-1} is ascribed to the N atoms embedded in the TiO_2 lattice, as illustrated in Fig. 6(b). This result clearly demonstrates that N is incorporated into the TiO_2 lattice. Nitridation transpires through the substitution of the oxygen atom in TiO_2 with the nitrogen atom from the urea molecule, resulting in the formation of the O-Ti-N bond (Selvaraj et al., 2013; Mehdizadeh et al., 2020; Khan et al., 2021). The intensity of the peaks at 1620 cm^{-1} and 775 cm^{-1} shifts to lower wavenumbers after Ag loading, which can be attributed to the asymmetric stretching vibration of the Ti-O-Ag bond (Suwarnkar et al., 2014).

A constraint of photocatalysts is the instability of excited electrons and their recombination with the generated holes. Hence, PL spectroscopy serves as an effective method for separating and measuring the electron-hole recombination rate and indicating the electronic structure of photocatalysts (Sirivallop et al., 2020). In this regard, PL spectroscopy is assessed for pure TiO_2 samples in comparison to TiO_2 doped with N and Ag. Fig. 7 illustrates the PL emission spectra for four TiO_2, 1.5 N-TiO_2, 0.5Ag-TiO_2, and Ag-N-TiO_2 samples. As shown in Fig. 7 the Ag-N-TiO_2, 0.5Ag-TiO_2, 1.5 N-TiO_2, and TiO_2 samples have lower peak intensity in the wavelength region of 475–540 nm and consequently have lower recombination rates. Therefore, the synergistic impact of N and Ag enhances the photocatalytic activity of TiO_2. Nitrogen enhances the electron-hole lifetime by trapping holes, and it has been proven if Ag ions reduce to Ag^0, functioning as an electron storage sink on the TiO_2 surface, can capture the photoexcited electrons. (Devi et al., 2012; Sirivallop et al., 2020; Khan et al., 2021). There is also the possibility of the formation of a junction between undoped and doped TiO_2, which reduces electron-hole recombination.

A fixed gas bed reactor is utilized for the photocatalytic reduction of CO_2. The photocatalytic efficacy of the prepared samples is assessed under visible light irradiation. Fig. 8(a) illustrates the generation of light hydrocarbon products resulting from the photocatalytic reduction of CO_2 over an 8-h period, utilizing a 250 W Hg lamp within the photoreactor. It should be noted that to prove the necessity of the simultaneous presence of photocatalyst, reactants, and light in the photocatalytic reduction of CO_2, several control experiments are designed and performed. These experiments include dark conditions with the photocatalyst in a CO_2 atmosphere, without CO_2 but with the photocatalyst in an N_2 atmosphere under light irradiation; without the photocatalyst but in the presence of CO_2 under light irradiation; and with pure PDMS polymer but in the presence of CO_2 under light irradiation. The results show that no hydrocarbon is produced in the absence of any of the main factors. These findings confirm that CO_2 is the only carbon source for the production of hydrocarbon products and there are no organic residues in the samples that can act as a carbon source. Consequently, this set of control experiments conclusively demonstrates that the simultaneous presence of a photocatalyst, reactants, and light irradiation is essential for the photocatalytic reduction of CO_2 to occur.

As observed in Fig. 8(a), methane and ethane are identified as the main gaseous products. The quantity of electrons and holes necessary for methane formation is inferior to that required for ethane, resulting in methane as the predominant product. The yield value of these two products is used as a criterion for assessing photocatalytic activity. Examination of the reaction mechanism reveals that when a photon with

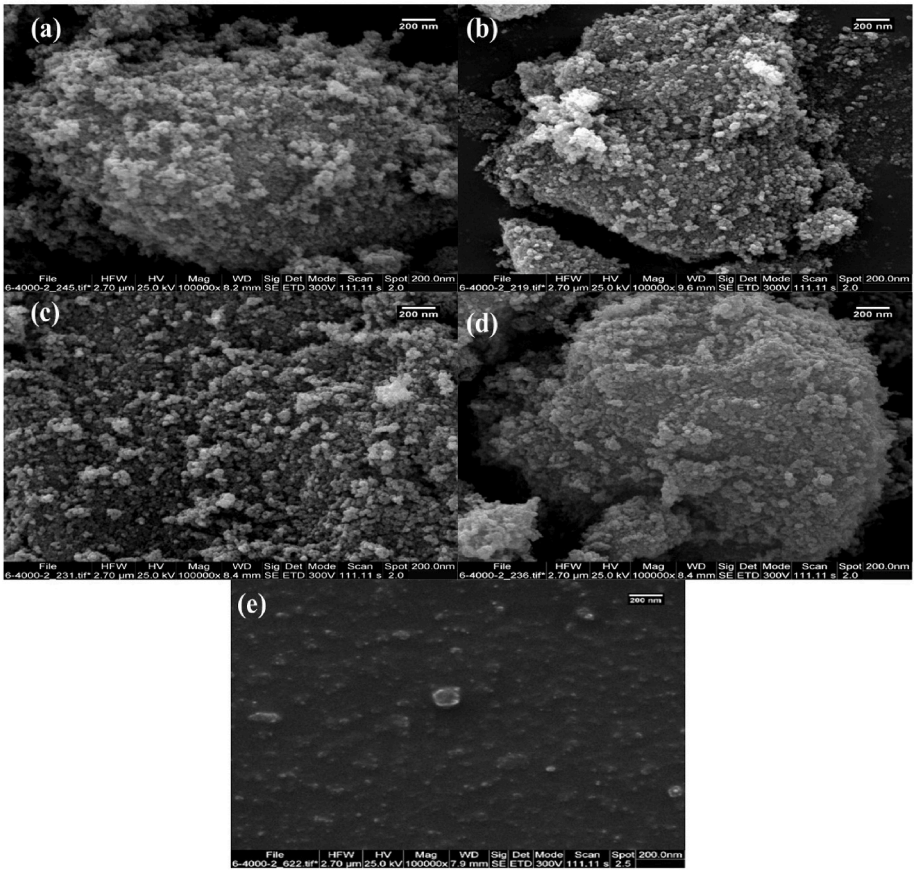

Fig. 3. FESEM images of (a) TiO_2, (b) 1.5 N-TiO_2, (c) 0.5Ag-TiO_2, (d) Ag-N-TiO_2, (e) PDMS-Ag-N-TiO_2 photocatalysts.

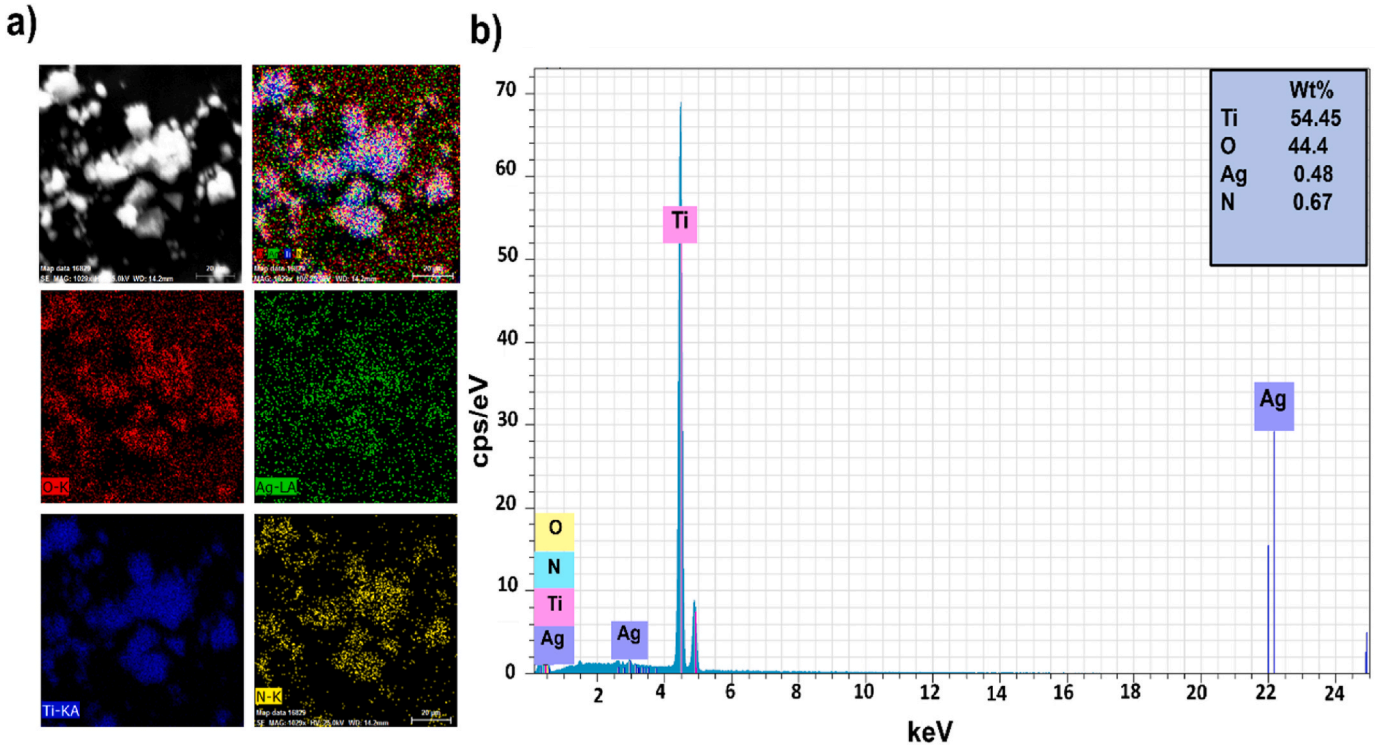

Fig. 4. (a) Mapping and (b) EDS analysis of the Ag-N-TiO_2 sample.

energy equal to or greater than the bandgap of the photocatalyst illuminates on TiO_2-based photocatalysts, it is absorbed and an electron

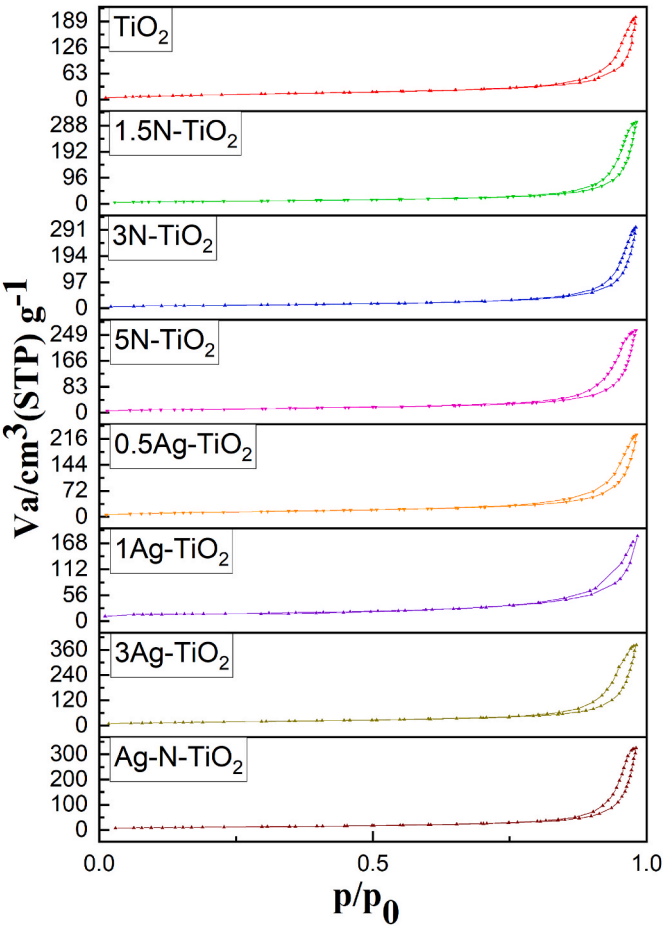

Fig. 5. N_2 adsorption-desorption isotherms for photocatalyst samples.

Table 2
Properties of photocatalysts measured BET analysis.

Photocatalyst	BET surface area (m^2/g)	Pore volume (cm^3/g)	Average pore diameter (nm)
TiO_2	40.16	0.50	50.04
1.5 N-TiO_2	66.62	0.59	35.54
3 N-TiO_2	62.17	0.28	18.26
5 N-TiO_2	49.98	0.35	28.13
0.5Ag-TiO_2	42.24	0.40	38.49
1Ag-TiO_2	39.38	0.46	47.22
3Ag-TiO_2	38.16	0.46	48.81
Ag-N-TiO_2	46.12	0.43	36.67

is transferred from the valence band to the conduction band, resulting in the formation of an exciton (electron-hole pair). Consequently, the free electron and hole generated after the exciton dissociation engage in reduction and oxidation reactions in the presence of reactants. The process of methane and ethane formation is described by:

$$h\nu + \text{PDMS\_Ag\_N\_TiO}_2 \rightarrow h^+_{VB} + e^-_{CB} \quad (3)$$

$$H_2O + 2h^+ \rightarrow \frac{1}{2}O_2 + 2H^+ \quad (4)$$

$$CO_2 + e^- \rightarrow CO_2^- \quad (5)$$

$$CO_2 + H^+ + e^- \rightarrow CO + OH^- \quad (6)$$

$$CO + H^+ + e^- \rightarrow C + OH^- \quad (7)$$

$$C + H^+ + e^- \rightarrow CH \quad (8)$$

$$CH + H^+ + e^- \rightarrow CH_2 \quad (9)$$

$$CH_2 + H^+ + e^- \rightarrow CH_3 \quad (10)$$

$$CH_3 + H^+ + e^- \rightarrow CH_4 \quad (11)$$

$$2\ .CH_3 \rightarrow C_2H_6 \quad (12)$$

As depicted in Fig. 8(a), due to the poor absorption of the undoped TiO_2 under the visible light, it exhibits negligible activity in the production of hydrocarbons. N-doped TiO_2 provides more reactions that the pure TiO_2 since it absorbs more photons because of its lower bandgap. Furthermore, the formed state in N-doped TiO_2 traps the photogenerated holes, reducing the recombination rate, which subsequently enhances the photocatalytic activity. The hydrocarbon production decreases as N-doping concentration increases. As the N-doping increases, a greater number of nitrogen atoms are incorporated within the TiO_2 lattice at the oxygen sites. However, given the differences in atomic diameter and valence electron count between N and O, an increased level of N-doping results in a decrease of active sites, disruption of stoichiometry, and an increase of the bandgap, which consequently diminishes photocatalytic activity. As reported, the increased N content on the catalyst surface results in the formation of electron-hole recombination centers, reducing the photocatalytic activity (Li et al., 2012). Among the N-doped samples, the 1.5 N-TiO_2 sample has the highest photocatalytic activity, with methane and ethane production of 28.29 and 1.1 μmol/g catalyst, respectively, which is consistent well with UV–vis and BET analyses.

According to Fig. 8(a), Ag-doping enhances the production of hydrocarbons in comparison with pure and N-doped TiO_2. However, among the three Ag-doping concentrations, the 0.5Ag-TiO_2 sample shows the highest activity, yielding methane and ethane hydrocarbons at values of 29.76 and 1.49 μmol/g of catalyst, respectively which are consistent with the optical and microstructure properties. Following the determination of the best percentages of N and Ag, the Ag-N-TiO_2 photocatalyst is prepared and assessed using photoreaction testing to determine the synergistic effects of co-doping. The photoreactor test results indicate a significant increase in hydrocarbon product yield in compared to all single-doped TiO_2 samples, proving the synergistic effect of N and Ag. These findings confirm the data obtained from UV–Vis and PL analyses, suggesting enhanced visible light absorption and more efficient exciton dissociation.

As another strategy, nanocomposite of Ag-N-TiO_2/PDMS is prepared and its photocatalytic performance is evaluated. As observed in Fig. 8 (a), a significant improvement in the performance of the co-doped TiO_2 is achieved when PDMS is employed as the support. Remarkably, the production of methane and ethane increases by approximately 2.8 and 10 times, respectively. This substantial increase can be attributed to several factors related to the properties of PDMS and its interaction with CO_2. PDMS exhibits an inherent affinity for CO_2 adsorption, making the photocatalytic system highly CO_2-philic. The chemical structure of PDMS contains siloxane bonds (Si-O-Si) that can interact with and adsorb CO_2 molecules. This interaction is characterized as an instantaneous quadrupole type. The CO_2 molecule, due to its linear structure, possesses a quadrupole moment with a partial positive charge on the carbon (C) atom and partial negative charges on the O atoms. The siloxane bonds (Si-O-Si) in PDMS can generate local electric field gradients due to the relative positive charge on the silicon atoms, resulting from the electronegativity difference between Si and O. This unique interaction between the quadrupole moment of CO_2 and the local electric field gradients in PDMS contributes to the polymer CO_2-philic nature and its enhanced CO_2 adsorption capability. The flexible Si-O backbone and low glass transition temperature of PDMS further augment its CO_2 adsorption properties. This interaction, combined with other

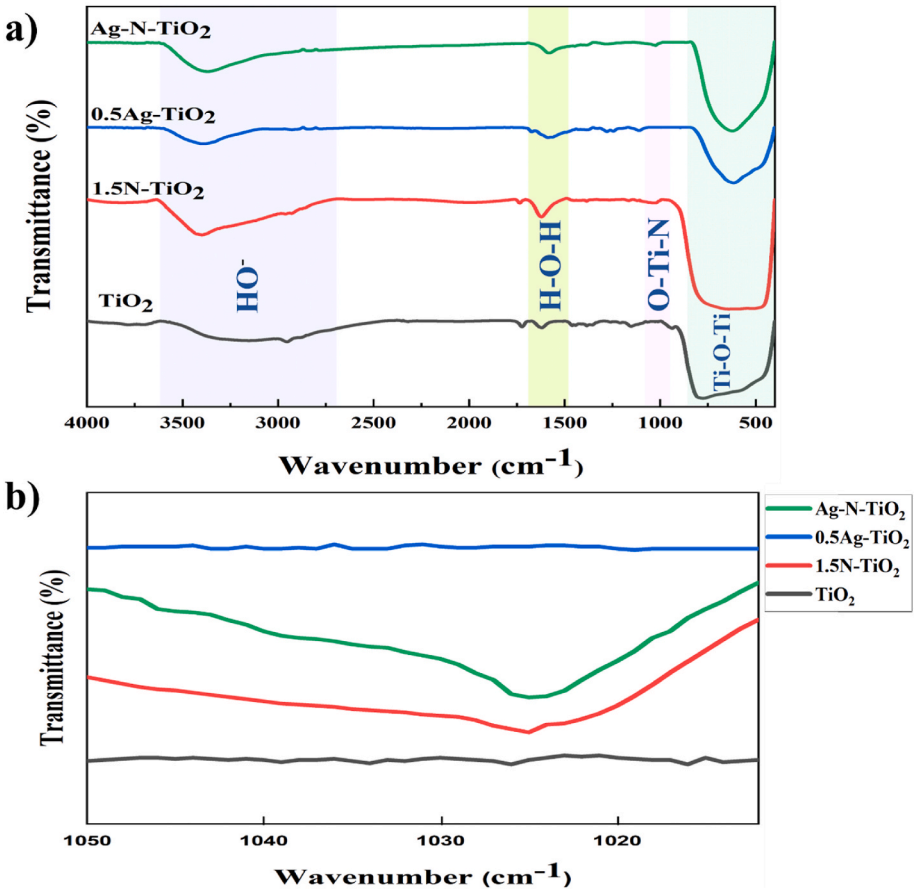

Fig. 6. (a) FTIR spectra of TiO_2 and doped TiO_2 (b) Magnified FTIR spectra of the samples in the range of 1050–1010 cm^{-1}.

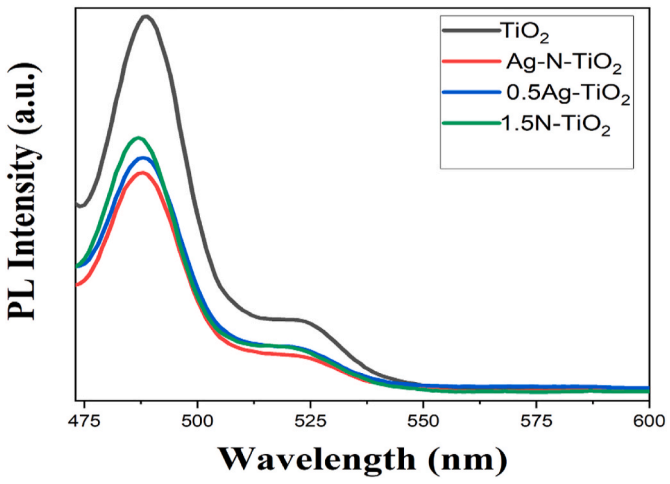

Fig. 7. PL spectra of pure TiO_2 and modified samples.

intermolecular forces, particularly van der Waals interactions, significantly increases the affinity of PDMS for CO_2 molecules. As a result of these interactions, the local concentration of CO_2 in the vicinity of the photocatalyst surface is substantially increased. This higher concentration of CO_2 leads to an enhanced availability of the reactant for the photocatalytic reduction process. This synergistic effect between the PDMS polymer and the Ag-N-TiO_2 photocatalyst demonstrates a promising approach for improving the efficiency of CO_2 photoreduction processes, potentially offering a more effective method for the conversion of CO_2 into valuable hydrocarbon products (Yoganathan et al., 2010; Rezakazemi et al., 2012; Genduso et al., 2019). It should be noted that the CO_2-philic nature of PDMS has also been supported by recent first-principles studies. Density functional theory (DFT) calculations have quantitatively demonstrated that CO_2 preferentially binds to siloxane (Si–O–Si) segments of PDMS through quadrupole-driven electrostatic interactions, with binding energies in the range of ~1–18 kcal/mol depending on polymer conformation and curvature. These studies further revealed that the local polarization induced by Si atoms enhances CO_2 quadrupole interactions, leading to increased adsorption affinity (Vaishnav et al., 2023).

The photocatalytic efficacy for the photoreduction of CO_2 is examined as a function of irradiation duration ranging from 0 to 8 h (Fig. 8 (b)). The time progression of the CO_2 conversion demonstrates that the yield of hydrocarbon products grows linearly with reaction time throughout the 8-h experiment, signifying the stability of the PDMS-Ag-N-TiO_2 sample during the reaction process. Also, the photocatalytic conversion of CO_2 to hydrocarbon products using the PDMS-Ag-N-TiO_2 sample is repeated three times, and the results are shown in Fig. 8(c). No significant change in the amount of methane and ethane production is observed in any of the tests, indicating that the PDMS-Ag-N-TiO_2 sample is stable under the present experimental conditions. Table 3 summarizes the comparative catalytic performance obtained in this study and those reported previously. While the PDMS-photocatalyst nanocomposite showed enhanced CO_2 photoreduction, several practical limitations should be noted. The performance depends on PDMS loading and distribution, and excessive polymer content may reduce effective light utilization and/or introduce mass transfer constraints; therefore, optimization of PDMS content is required. In addition, experiments were conducted in a laboratory scale reactor, so further engineering assessment is needed for scale-up and continuous operation.

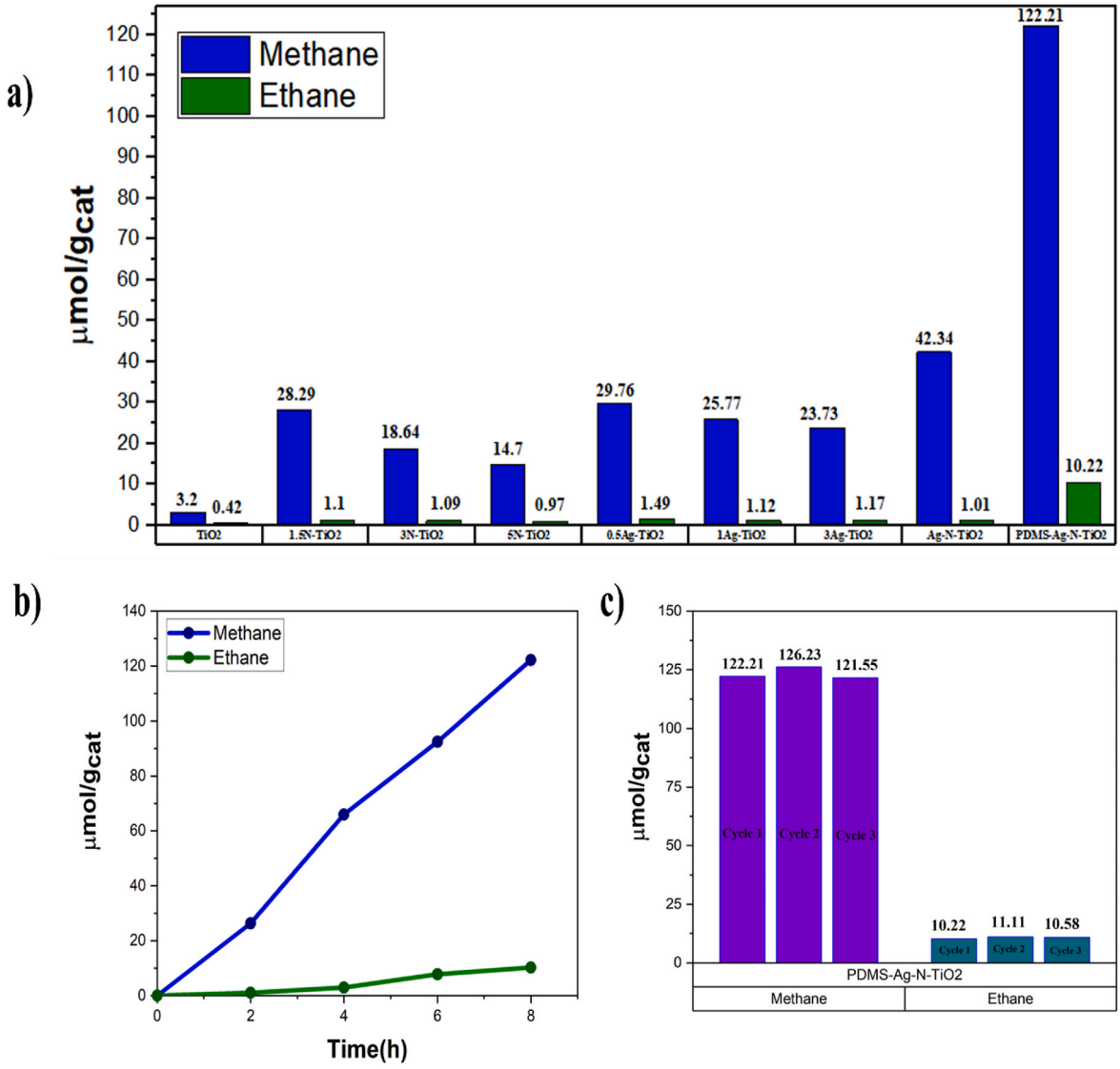

Fig. 8. (a) Yield of hydrocarbon products through the photocatalytic reduction of CO_2 using different photocatalysts (b) Methane and ethane yield for PDMS-Ag-N-TiO_2 sample over 8 h of reaction (c) Stability of PDMS-Ag-N-TiO_2 sample during three photocatalytic reaction cycles.

Table 3
Photocatalyst performance comparison with materials reported in the literature.

Photocatalyst	Product yield	Experimental Condition	Reference
TiO_2	0.33 (µmol/g.h) CH_4	CO_2 gas with H_2O, gas-phase batch, 250 W (Hg lamp), 25 °C and 1 atm	(Moradi et al., 2020)
(001)TiO_2-gC_3N_4/$BiVO_4$	0.5 (µmol/g.h) CH_4 15.2 (µmol/g.h) CO	CO_2 gas with H_2O, gas-phase batch, 300 W Xe lamp, 25 °C and 1 atm	(Bian et al., 2021)
Pt@$BiVO_4$/TiO_2	4.96 (µmol/g.h) CH_4	CO_2 gas with H_2O, gas-phase batch, 250 W (Hg lamp), 40 °C and 1 atm	(Ahmadi et al. 2024)
Au/TiO_{2-x}	3.30 (µmol/g.h) CH_4 0.66 (µmol/g.h) C_2H_6	batch reactor, 1 bar, 2:7 water vapor/CO_2, 50 W LED	(Wang et al., 2021)
S@ZnO/TiO_2	16.67 (µmol/g.h) CH_4	CO_2 gas with H_2O, gas-phase batch, 200 W Hg/Xe lamp	(Al-Hajji et al., 2025)
PDMS-Ag-N-TiO_2	15.27 (µmol/g.h) CH_4 1.27 (µmol/g.h) C_2H_6	CO_2 gas with H_2O, gas-phase batch, 250 W (Hg lamp), 40 °C and 1 atm	This work

4. Conclusions

This work addresses the current gap in the development of flexible, low-cost, visible-light-active TiO_2-based photocatalytic systems capable of efficiently convertion of CO_2 into valuable hydrocarbons. Using Ag and N co-doping strategy for TiO_2 and dispersing it in transparent, flexible, stable, and CO_2-philic PDMS, a photocatalytic nanocomposite was achieved that showed a high yield for conversion of CO_2 into methane and ethane. First, the Ag-doped and N-doped TiO_2 with different concentrations of the doping agents were prepared and their crystallinity, optical properties, and microstructural properties were investigated. As revealed, Ag and N doping reduced the band gap of TiO_2, making them visible-active. Using a fix-bed photoreactor to evaluate the photocatalytic performance, 1.5-N-TiO_2 and 0.5-Ag-TiO_2 resulted in the highest production yield for conversion of CO_2 into the methane and ethane. These doping concentrations were employed for co-doing of TiO_2 which resulted in the significant improvement in the conversion of CO_2 into the hydrocarbons. Ag-N-TiO_2 achieved 34.42 and 1.01 µmol/g catalyst yield values for methane and ethane, respectively. To make the photocatalyst more applicable and efficient, nanocomposite of Ag-N-TiO_2 and PDMS was prepared. Remarkably, when the PDMS-Ag-N-TiO_2 nanocomposite is employed, the highest methane and

ethane yeilds of 122.21 and 10.22 μmol/g catalyst were achieved, respectively. PDMS promoted the adsorption of greater amounts of CO_2 on the photocatalyst surface, making it more available for the photocatalytic reduction reaction and thereby enhancing hydrocarbon production. This research presented a promising approach for improving the efficiency of CO_2 conversion processes to valuable fuels, potentially contributing to environmental pollution reduction and sustainable energy resource development. The findings also highlight the broader potential of polymer-photocatalyst hybrid systems for integration into practical photoreactors. Future work should focus on quantitatively characterizing polymer-CO_2 interactions, optimizing the composition and thickness of the nanocomposite layers and exploring the performance of such systems under real solar irradiation and more realistic process conditions.

CRediT authorship contribution statement

Majed Bahadorian: Writing – original draft, Methodology, Investigation, Formal analysis, Data curation. **Farzaneh Arabpour Roghabadi:** Writing – review & editing, Supervision, Methodology, Investigation, Conceptualization. **Vahid Ahmadi:** Validation, Methodology, Conceptualization. **Afsanehsadat Larimi:** Writing – review & editing, Methodology, Formal analysis.

Declaration of competing interest

The authors declare that they have no known competing financial interests or personal relationships that could have appeared to influence the work reported in this paper.

Data availability

No data was used for the research described in the article.

References

Ahmadi, M., Alavi, S.M., Larimi, A., 2023. UV–vis light responsive Bi_2WO_6 nanosheet/TiO_2 nanobelt heterojunction photo-catalyst for CO_2 reduction. Catal. Commun. 179, 106681.

Ahmadi, M., Alavi, S.M., Larimi, A., 2024a. Effective CO_2 photoreduction to methane over Bi_2MoO_6/Ni, N co-doped TiO_2 nano-photocatalyst. Int. J. Hydrogen Energy 56, 1309–1323.

Ahmadi, M., Alavi, S.M., Larimi, A., 2024b. Highly active platinum decorated $BiVO_4$ nanosheet/TiO_2 nanobelt heterojunction for photocatalytic CO_2 reduction. Surf. Interfaces 45, 103908.

Al-Hajji, L., Ismail, A.A., Alsaidi, M., Nazeer, A.A., El-Toni, A.M., Al-Ruwayeh, S., Ahmed, S., Al-Sharrah, T., 2025. Fabrication of mesoporous sulfated ZnO-modified g-C_3N_4 and TiO_2 photocatalysts for CO_2 reduction in gas phase. Catal. Today 445, 115089.

Ali, H.M., Arabpour Roghabadi, F., Ahmadi, V., Amjadi, A., Ghaedi, I., 2024. Wastewater treatment using high-performance in situ formed double-heterojunction janus photocatalyst microparticles shaped via a microfluidic device. Langmuir 40 (27), 13968–13983.

Ali, H.M., Roghabadi, F.A., Ahmadi, V., 2023. Solid-supported photocatalysts for wastewater treatment: supports contribution in the photocatalysis process. Sol. Energy 255, 99–125.

Asadi, A., Larimi, A., Jiang, Z., Naderifar, A., 2022. Modeling and simulation of photocatalytic CO_2 reduction into methanol in a bubble slurry photoreactor. Chem. Eng. Sci. 263, 118078.

Bahadorian, M., Bahadorian, A., Pourdelan, H., Ebadi, T., Kowsari, E., 2025. Photocatalytic performance of B-gC_3N_4/BiOCl nanocomposite in Rhodamine B degradation for water treatment: synthesis, characterization, and optimization. Appl. Catal.: Open, 207076.

Beshtar, M., Asgharinezhad, A.A., Larimi, A., 2024. Ultra-deep photocatalytic oxidative desulfurization of liquid fuels by Ti@ CeO_2/ZnO nanophotocatalyst under visible light and mild operating conditions. J. Ind. Eng. Chem. 134, 548–560.

Bhatkhande, D.S., Pangarkar, V.G., Beenackers, A.A.C.M., 2002. Photocatalytic degradation for environmental applications–a review. J. Chem. Technol. Biotechnol. Int. Res. Process Environ. Clean Technol. 77 (1), 102–116.

Bian, J., Zhang, Z., Feng, J., Thangamuthu, M., Yang, F., Sun, L., Li, Z., Qu, Y., Tang, D., Lin, Z., 2021. Energy platform for directed charge transfer in the cascade Z-scheme heterojunction: CO_2 photoreduction without a cocatalyst. Angew. Chem. 133 (38), 21074–21082.

Cheng, X., Yu, X., Xing, Z., Yang, L., 2016. Synthesis and characterization of N-doped TiO_2 and its enhanced visible-light photocatalytic activity. Arab. J. Chem. 9, S1706–S1711.

Cui, Y., Ge, P., Chen, M., Xu, L., 2022. Research progress in semiconductor materials with application in the photocatalytic reduction of CO_2. Catalysts 12 (4), 372.

Deng, L., Chang, B., Shi, D., Yao, X., Shao, Y., Shen, J., Zhang, B., Wu, Y., Hao, X., 2021. MXene decorated by phosphorus-doped TiO_2 for photo-enhanced electrocatalytic hydrogen evolution reaction. Renew. Energy 170, 858–865.

Deshmukh, S.B., Deshmukh, K.H., Mane, M.L., Mane, D.V., 2021. Effect of Nitrogen Doping on Structural and Optical Properties of TiO_2 Nanoparticles. Wiley Online Library, Macromolecular Symposia.

Devi, L.G., Nagaraj, B., Rajashekhar, K.E., 2012. Synergistic effect of Ag deposition and nitrogen doping in TiO_2 for the degradation of phenol under solar irradiation in presence of electron acceptor. Chem. Eng. J. 181, 259–266.

Diao, W., Xu, J., Rao, X., Zhang, Y., 2022. Facile synthesis of fluorine doped rutile TiO_2 nanorod arrays for photocatalytic removal of formaldehyde. Catal. Lett. 152 (4), 1029–1039.

Divya, G., Jaishree, G., Rao, T.S., Chippada, M.P., Lakshmi, K.D., Supriya, S.S., 2022. Improved catalytic efficiency by N-doped TiO_2 via sol gel under microwave irradiation: dual applications in degradation of dye and microbes. Hybrid Adv. 1, 100010.

Garcia, A.E., Sanito, R.C., Gao, M., Chuang, S.S., Azizah, L.A.N., 2025. Advances in non-thermal and electrochemical CO_2 conversion technologies towards net-zero emissions. Clean. Eng. Technol., 100944

Gegova, R., Bachvarova-Nedelcheva, A., Iordanova, R., Dimitriev, Y., 2015. Synthesis and crystallization of gels in the TiO_2-TeO_2-ZnO system. Bulg. Chem. Commun. 47 (1), 378–386.

Genduso, G., Litwiller, E., Ma, X., Zampini, S., Pinnau, I., 2019. Mixed-gas sorption in polymers via a new barometric test system: sorption and diffusion of CO_2-CH_4 mixtures in polydimethylsiloxane (PDMS). J. Membr. Sci. 577, 195–204.

Guo, F., Sun, H., Huang, X., Shi, W., Yan, C., 2020. Fabrication of TiO2/high-crystalline g-C3N4 composite with enhanced visible-light photocatalytic performance for tetracycline degradation. J. Appl. Chem. Biotechnol. 95 (10), 2684–2693.

Jahdi, M., Mishra, S.B., Nxumalo, E.N., Mhlanga, S.D., Mishra, A.K., 2020. Smart pathways for the photocatalytic degradation of sulfamethoxazole drug using F-Pd co-doped TiO_2 nanocomposites. Appl. Catal. B Environ. 267, 118716.

Janani, B., Sre, V.V., Syed, A., Elgorban, A.M., Abid, I., Wong, L.S., Khan, S.S., 2025. Constructing bifunctional interfacial electric field triggered $NiCo_2S_4$ loaded 3D nanoflower CuFe LDH as self-cascade nanoreactor photo-Fenton system to efficiently degrade ciprofloxacin. Surf. Interfaces 64, 106289.

Jing, Y., Yin, H., Li, C., Chen, J., Wu, S., Liu, H., Xie, L., Lei, Q., Sun, M., Yu, S., 2022. Fabrication of Pt doped TiO_2–ZnO@ ZIF-8 core@ shell photocatalyst with enhanced activity for phenol degradation. Environ. Res. 203, 111819.

Kang, S., Hwang, J., 2022. rGO-wrapped Ag-doped TiO_2 nanofibers for photocatalytic CO_2 reduction under visible light. J. Clean. Prod. 374, 134022.

Karunakaran, C., Anilkumar, P., Gomathisankar, P., 2011. Photoproduction of iodine with nanoparticulate semiconductors and insulators. Chem. Cent. J. 5, 1–9.

Khairy, M., Kamar, E., Mousa, M., 2022. Photocatalytic activity of nano-sized Ag and Au metal-doped TiO_2 embedded in rGO under visible light irradiation. Mater. Sci. Eng., B 286, 116023.

Khan, S.S., Steffy, J., Alfagham, A.T., Elgorban, A.M., 2025. Stabilize the oxygen vacancies in $LaFeO_3$ via altering local electronic structure with CeO_2 and WS2 QDs: a novel strategy for achieving durable visible light driven photoinactivation. J. Water Proc. Eng. 71, 107174.

Khan, T.T., Bari, G.A.R., Kang, H.-J., Lee, T.-G., Park, J.-W., Hwang, H.J., Hossain, S.M., Mun, J.S., Suzuki, N., Fujishima, A., 2021. Synthesis of N-doped TiO_2 for efficient photocatalytic degradation of atmospheric NOx. Catalysts 11 (1), 109.

Li, H., Hao, Y., Lu, H., Liang, L., Wang, Y., Qiu, J., Shi, X., Wang, Y., Yao, J., 2015. A systematic study on visible-light N-doped TiO_2 photocatalyst obtained from ethylenediamine by sol–gel method. Appl. Surf. Sci. 344, 112–118.

Li, X., Zhuang, Z., Li, W., Pan, H., 2012. Photocatalytic reduction of CO_2 over noble metal-loaded and nitrogen-doped mesoporous TiO_2. Appl. Catal. Gen. 429, 31–38.

Marques, J., Gomes, T.D., Forte, M.A., Silva, R.F., Tavares, C.J., 2019. A new route for the synthesis of highly-active N-doped TiO_2 nanoparticles for visible light photocatalysis using urea as nitrogen precursor. Catal. Today 326, 36–45.

Mehdizadeh, P., Tavangar, Z., Shabani, N., Hamadanian, M., 2020. Visible light activity of nitrogen-doped TiO_2 by sol-gel method using various nitrogen sources. Journal of Nanostructures 10 (2), 307–316.

Moradi, M., Khorasheh, F., Larimi, A., 2020. Pt nanoparticles decorated Bi-doped TiO_2 as an efficient photocatalyst for CO_2 photo-reduction into CH_4. Sol. Energy 211, 100–110.

Nagaraj, G., Mohammed, M.K., Abdulzahraa, H.G., Sasikumar, P., Karthikeyan, S., Tamilarasu, S., 2021. Effects of the surface of solar-light photocatalytic activity of Ag-doped TiO_2 nanohybrid material prepared with a novel approach. Appl. Phys. A 127 (4), 269.

Piątkowska, A., Janus, M., Szymański, K., Mozia, S., 2021. C-, N-and S-doped TiO_2 photocatalysts: a review. Catalysts 11 (1), 144.

Raguram, T., Rajni, K., 2022. Synthesis and characterisation of Cu-Doped TiO_2 nanoparticles for DSSC and photocatalytic applications. Int. J. Hydrogen Energy 47 (7), 4674–4689.

Rezakazemi, M., Shahidi, K., Mohammadi, T., 2012. Sorption properties of hydrogen-selective PDMS/zeolite 4A mixed matrix membrane. Int. J. Hydrogen Energy 37 (22), 17275–17284.

Safa, M.B., Steffy, J., Syed, A., Subhiksha, V., Elgorban, A.M., Verma, M., Wong, L.S., Khan, S.S., 2025. Unveiling the enhanced rhodamine B degradation in water by

Sn_3O_4@ Au: insight into degradation pathway and by-products toxicity evaluation. J. Water Proc. Eng. 72, 107475.
Santos, L.M., Machado, W.A., França, M.D., Borges, K.A., Paniago, R.M., Patrocinio, A.O., Machado, A.E., 2015. Structural characterization of Ag-doped TiO_2 with enhanced photocatalytic activity. RSC Adv. 5 (125), 103752–103759.
Saravanan, A., Vo, D.-V.N., Jeevanantham, S., Bhuvaneswari, V., Narayanan, V.A., Yaashikaa, P., Swetha, S., Reshma, B., 2021. A comprehensive review on different approaches for CO_2 utilization and conversion pathways. Chem. Eng. Sci. 236, 116515.
Selvaraj, A., Parimiladevi, R., Rajesh, K., 2013. Synthesis of nitrogen doped titanium dioxide (TiO_2. J. Environ. Nanotechnol 2 (1), 35–41.
Sirivallop, A., Areerob, T., Chiarakorn, S., 2020. Enhanced visible light photocatalytic activity of N and Ag doped and co-doped TiO_2 synthesized by using an in-situ solvothermal method for gas phase ammonia removal. Catalysts 10 (2), 251.
Sosnin, I.M., Vlassov, S., Dorogin, L.M., 2021. Application of polydimethylsiloxane in photocatalyst composite materials: a review. React. Funct. Polym. 158, 104781.
Sre, V.V., Syed, A., Janani, B., Elgorban, A.M., Al-Shwaiman, H.A., Wong, L.S., Verma, M., Khan, S.S., 2025. Unveiling the enhanced rifampicin degradation in water by Ni/Fe dual anchored tubular gC_3N_4 as a peroxymonosulfate activator: insight into mechanism, degradation pathway and by-products toxicity evaluation. J. Water Proc. Eng. 79, 108983.
Srikanth, B., Goutham, R., Narayan, R.B., Ramprasath, A., Gopinath, K., Sankaranarayanan, A., 2017. Recent advancements in supporting materials for immobilised photocatalytic applications in waste water treatment. J. Environ. Manag. 200, 60–78.
Steffy, J., Syed, A., Janani, B., Al-Shwaiman, H.A., Wong, L.S., Verma, M., Khan, S.S., 2025a. Defect engineering of sulfur vacancies in $ZnIn_2S_4$ nanoflower integrated with Ag^0 in $NaBH_4$ activation toward organic contaminates degradation: critical role of Cu^{2+} and mechanism insight. J. Water Proc. Eng. 75, 108057.
Steffy, J., Syed, A., Janani, B., Jitesh, V., Bahkali, A.H., Elgorban, A.M., Balakrishnaraja, R., Wong, L.S., Verma, M., Khan, S.S., 2025b. Establishment of tandem hybrid system by the deposition of Ag NPs on Sn-incorporated spinel ferrite for rapid catalytic and peroxymonosulfate activated photocatalytic degradation of organic pollutants in aqueous media. Surf. Interfaces, 108084.
Subhiksha, V., Syed, A., Janani, B., Elgorban, A.M., Abid, I., Wong, L.S., Khan, S.S., 2025. Topotactic synthesis of Fe_3O_4 decorated N-doped BiOBr for enhanced photocatalytic degradation of bromoxynil. Int. J. Hydrogen Energy 97, 882–890.
Sun, L., Haidry, A.A., Fatima, Q., Li, Z., Yao, Z., 2018. Improving the humidity sensing below 30% RH of TiO_2 with GO modification. Mater. Res. Bull. 99, 124–131.
Suwarnkar, M., Dhabbe, R., Kadam, A., Garadkar, K., 2014. Enhanced photocatalytic activity of Ag doped TiO_2 nanoparticles synthesized by a microwave assisted method. Ceram. Int. 40 (4), 5489–5496.
Tahir, M., Tahir, B., 2016. Dynamic photocatalytic reduction of CO_2 to CO in a honeycomb monolith reactor loaded with Cu and N doped TiO_2 nanocatalysts. Appl. Surf. Sci. 377, 244–252.
Vaishnav, A., Fujikawa, S., Staykov, A., 2023. Curvature effect in polydimethylsiloxane interaction with CO_2. Insights from theory. J. Phys. Chem. 127 (4), 876–885.
Wang, K., Lu, J., Lu, Y., Lau, C.H., Zheng, Y., Fan, X., 2021. Unravelling the CC coupling in CO_2 photocatalytic reduction with H_2O on Au/TiO_{2-x}: combination of plasmonic excitation and oxygen vacancy. Appl. Catal. B Environ. 292, 120147.
Wang, W., Xu, D., Cheng, B., Yu, J., Jiang, C., 2017. Hybrid carbon@ TiO_2 hollow spheres with enhanced photocatalytic CO_2 reduction activity. J. Mater. Chem. A 5 (10), 5020–5029.
Wang, Z., Cai, W., Hong, X., Zhao, X., Xu, F., Cai, C., 2005. Photocatalytic degradation of phenol in aqueous nitrogen-doped TiO_2 suspensions with various light sources. Appl. Catal. B Environ. 57 (3), 223–231.
Yoganathan, R., Mammucari, R., Foster, N., 2010. Dense gas processing of polymers. Polym. Rev. 50 (2), 144–177.
Yuan, Y., Ding, J., Xu, J., Deng, J., Guo, J., 2010. TiO_2 nanoparticles co-doped with silver and nitrogen for antibacterial application. J. Nanosci. Nanotechnol. 10 (8), 4868–4874.
Zhang, H., Jiang, Y., Zhou, B., Wei, Z., Zhu, Z., Han, L., Zhang, P., Hu, Y., 2021. Preparation and photocatalytic performance of silver-modified and nitrogen-doped TiO_2 nanomaterials with oxygen vacancies. New J. Chem. 45 (10), 4694–4704.
Zheng, Y.-T., Li, S., Huang, N.-Y., Li, X., Xu, Q., 2024. Recent advances in metal–organic framework-derived materials for electrocatalytic and photocatalytic CO_2 reduction. Coord. Chem. Rev. 510, 215858.